An x-ray transmission grating spectrometer for Lynx

Hans M. Günther[a] and R. K. Heilmann[a]

[a]Massachusetts Institute of Technology, Cambridge, MA, US

ABSTRACT

NASA commissioned four studies for large astrophysics missions in different wavebands to provide input for the 2020 Decadal Survey of Astronomy and Astrophysics. The X-ray concept under study is called "Lynx". The Lynx Science and Technology Definition Team has formulated science requirements and we need to evaluate the optical technologies that can meet these requirements. In this context, we present a draft design for a Lynx X-ray grating spectrometer (XGS) using critical-angle transmission (CAT) gratings on a Rowland torus. One of the most important parameters for the achievable spectral resolving power R is the mirror point-spread function (PSF). Different mirror technologies can lead to different PSF characteristics, e.g. the PSF might be dominated by scattering and figure errors or by the misalignment of many different mirror shells. The benefits of using sub-apertures to increase the resolving power could differ widely between different scenarios. Our study avoids mirror-specific assumptions and looks at how we can adjust the design to any of the proposed technologies.

Size and placement of the CAT gratings have strong impact on spectral resolving power. We show how gratings can be arranged to meet the Lynx requirements. One consideration is how the presence of gratings impacts the effective area of the zeroth order. We discuss and trade-offs between resolving power and effective area in our design that can be adjusted to match the science requirements.

Keywords: ray-tracing, X-ray optics, critical angle transmission grating, Lynx, Rowland design

1. INTRODUCTION

When we look at the big questions in astrophysics, we inevitably will be drawn to dramatic and energetic events such as those associted with galactic feedback, the dawn of black holes, and the dynamic accretion and outburst events in star formaing regions. Often, X-rays are the best (and in some cases the only) waveband to observe the hot and energetic universe. Due to the Earth's atmosphere, early X-ray observations were limited by the short flights of instruments on ballons or sounding rockets, but a series of exceptionally sucessful satellites has driven the field forward in the last few decades. In particular, our understanding of X-ray emission from astrophysical sources has been revolutionized by the launch of XMM-Newton and Chandra with their high spectral and spatial resolution. Both were launched at the end of the last millenium (in 1999) as an ESA Horizon 2000 cornerstone mission and a NASA Great Observatory, respectively. Both missions are still operating and continue to deliver magnificent data. However, while they increased resolving power and effective area significantly above what was available before, we need another leap in capability to identify "the invisible drivers of galaxy formation", understand "the dawn of black holes", and "the Energetic Side of Stellar Evolution and Stellar Ecosystems" – these are the headlines for the Lynx science case. On the ESA side, there is a sucessor misson, Athena,[1,2] under development. Athena will feature a large collecting area of order 1.5 m^2, but with a point-spread-function (PSF) of several arcseconds. It will be equipped with a mirocalorimeter and a wide-field-imager.

As preparation for the 2020 Decadal Survey, NASA has comissioned a study for a large X-ray mission. The concept for this mission is currently called "Lynx" and it is planned to enable key-science which cannot be done with Athena. In particular, "Lynx" will have a much narrower PSF with a half-power-diameter (HPD) of only 0.5 arcsec, and a diffraction grating spectrometer is one of three candidate science instruments.[3] While micro-calorimeters are superior to grating spectroscopy for high-energies, in soft X-rays (in the following we will use this term to mean X-rays below 2 keV) dispersion gratings are unmatched in resolving power. The

Send correspondence to H.M.G.
E-mail: hgunther@mit.edu

Space Telescopes and Instrumentation 2018: Ultraviolet to Gamma Ray, edited by Jan-Willem A. den Herder, Shouleh Nikzad, Kazuhiro Nakazawa, Proc. of SPIE Vol. 10699, 1069914 · © 2018 SPIE
CCC code: 0277-786X/18/$18 · doi: 10.1117/12.2314054

Lynx Science and Technology Definition Team has defined the following minimum requirements for a Lynx X-ray grating spectrometer (XGS): Around the wavelength of the density and temperature sensitive O VII triplet (about 0.6 keV), which provides an important diagnostic in several fields, the XGS shall deliver a resolving power $R > 5000$ and an effective area $A_{\rm eff} > 4000$ cm^2. In this paper we describe one possible design for the XGS that could deliver these requirements; just to be conservative in these early stages, we plan to exceed both requirements by at least 10%. In this design, we make use of transmission gratings that are mounted blazed as "critical angle transmission (CAT)" gratings.[4,5] CAT gratings have a significantly higher grating efficiency compared with the transmission gratings used in Chandra. Alternatively, off-plane reflection gratings could be used and a design for those is discussed by McEntaffer et. al. in this volume.

A general overview of the Lynx mission is given in reference 3 and updated by Gaskin et al. in this volume. CAT gratings have been described before[4,5] and recent development progress is discussed by Heilmann et al. in this volume in the context of the Arcus explorer mission.[6] In this paper, we describe the properties of the Lynx mission and of CAT gratings that are the most important for the design of the XGS and for our ray-trace simulations (section 2). In section 3 we explain the geometry of the spectrometer before we show the setup of our ray-trace simulations in section 4. Ray-tracing results are shown in section 5. We discuss several design options in section 6 and end with a short summary (section 7).

2. BOUNDARY CONDITIONS FOR THE SPECTROMETER DESIGN

In this section, we examine the input parameters for the design of the spectrometer and our ray-traces.

2.1 Lynx mirrors

Three different mirror technologies are under consideration for Lynx, all are planned for a focal length of 10 m. Until a specific techology is chosen, we perform simulations without a detailed mirror model. Instead, we use an effective model, where we simulate a perfect mirror that focusses all rays from an on-axis source exactly to the focal point and then apply scattering to broaden the PSF to 0.5 arcsec HPD. This scatter can be applied in the plane of reflection or perpendicular to the plane of reflection (also called "out of plane"). If the mirror is made up of many different shells and each of those shells has a very sharp PSF, but they are misalinged with respect to each other, we need to run simulations where in-plane and out-of-plane scatter contribute equally. If instead the mirror shells are well aligned, and the dominant broadening mechanism of the PSF is the figure error or scattering by particulates, the in-plane scatter should be larger than the out-of-plane scatter. In this case, sub-aperturing of the aperture as discussed below can improve the spectral resolving power. We run simulations for both cases.

The most important property of the mirror however is the effective area at different energies. These simulations assume tabulated values that are distributed by the Lynx study office for design purposes; for a geometric ray-trace as we want to perform here we have to assume some geometric configuartion (size, position) of the mirror. For most of our results however, changing the $A_{\rm eff}$ of the mirror at some energy just acts as an overall scale factor for the $A_{\rm eff}$ of the XGS at that energy. There is some influcence on R since the astigmatism depends on the physical dimensions, but this is not the dominating effect, as shown below. Thus, to first order, changes in the mirror parameters will not lead to fundamental design changes of the XGS presented here.

2.2 CAT gratings

Critical angle transmission (CAT) gratings are etched from thin Si wavers with a high aspect ratio.[4,5] The gratings are used with a blaze angle, meaning that the incoming photons are not parallel to the sides of the grating bars, but hit them at an angle below the critical angle. This causes photons to be preferentially diffracted to one side. The peak of the distribution of diffracted photons is at about twice the blaze angle. The critical angle depends on the material of the grating. Here, we consider pure Si and Si that is coated with Pt. The grating effiency (the probability that a photon of a certain energy and angle is diffracted into a specific order) further depends on the geometric dimension of the grating bars. For the simulations here we assume gratings that are 5.7 μm deep with a grating period of 200 nm and a 140 μm open gap between the bars. The grating bars are supported by Si bars running perpendicular to them (L1 support structure) and the combined structure of grating bars and L1 support sits on top of 1 mm wide hexagons (L2 support structure). We assume that

L1 and L2 cover about 10% of the geometric area each and reduce the photon throughput accordingly. We simulate different sizes for grating membranes surrounded by a mounting frame (together called a "facet") up to 50 mm × 50 mm. Most of these properties are better than the gratings manufactured so far, but they are certainly achievable with some development effort. For example, the L1 and L2 structures in gratings manufactured so far typically cover 15% and 19% of the area, but the gratings have survived extensive environmental testing with no damage[5] (see also Heilmann at al. in this volume), indicating that these structures could be made thinner without a significant impact on stability.

2.3 CCDs

The dispersed spectrum needs to be detected with a device that is sensitive to the photon energy because several orders of the dispersed spectrum will overlap. Moderate energy resolution is sufficient to assign detected events to a particular order. In our simulations we baseline charge-coupled devices that are approximately 50 mm × 25 mm large and have 2048 × 1024 pixels. Such CCDs are planned for the Arcus mission.[6]

2.4 Filters

CCDs are sensitve to optical and UV light and thus optical blocking filters need to be added to the design. For the simulations here we assume a 30 nm layer of Al topped with 10 nm of aluminum oxide, which may be directly deposited on the CCDs, and 45 nm of Kapton mounted on a metal mesh with 95% transmissivity.

3. LAYOUT OF SPECTROGRAPH

We design the spectrograph to follow the Rowland geometry.[7] All gratings are positioned on the surface of the Rowland torus where we chose the dimension of the torus such that the gratings are close to the mirrors because a longer distance improves the spectral resolving power. The optical axis does not pass through the center of the Rowland circle, instead, the entire torus is tilted.[8,9] We orient the gratings such that a ray coming through the center of the grating has the prescribed blaze angle (1.6 degrees in our design). Since the grating is flat and the torus is curved, most points on the grating do not match the Rowland torus exactly. Using a geometry with a tilted torus reduces the average difference.

The CCDs are also placed on the Rowland torus. We determine the best position and the required number of CCDs below. For CAT gratings, most of the diffracted power is found around twice the blaze angle. In addition, the zeroth order must be covered by a detector since the distance between the zeroth order and the diffracted signals is essential for wavelength calibration. Also, since the gratings mostly disperse soft X-rays, signal at the positions of the zeroth-order can be used for imaging spectroscopy with the energy resolution of the detector. In the case of Lynx, we plan to use the microcalorimater as the primary zeroth-order detector for use with the grating spectrograph. Since the microcalorimater is operated at very low temperatures, it must be mounted in a dewar with a radius around 390 mm. The CCD that detect the diffracted signal thus must be placed at a larger distance.

We can write the equation of a torus that is not tilted as

$$\begin{pmatrix} x \\ y \\ z \end{pmatrix} = \begin{pmatrix} (R + r\cos\theta)\cos\varphi \\ r\sin\theta \\ (R + r\cos\theta)\sin\varphi \end{pmatrix} \quad . \tag{1}$$

When we talk about the "Rowland circle", we mean the points that fulfill equation 1 with $\theta = 0$, which gives us a circle in the (x,z) plane. This equation can be generalized to tori where the center $\vec{c}$ does not coincide with the origin of the coordinate system and the axis of symmetry is not parallel to one of the axes of the coordinate system. The axis of symmetry is given by a unit vector $\vec{e}_y$. We define a vector $\vec{e}_R(\varphi) = \vec{e}_x \cos\varphi + \vec{e}_z \sin\varphi$ and can now write a generalized torus equation for points $\vec{p}$:

$$\vec{p}(\varphi,\theta) = \vec{c} + R\,\vec{e}_R(\varphi) + r\,(\vec{e}_y \sin\theta + \vec{e}_R(\varphi)\cos\theta) \quad . \tag{2}$$

For a torus that is translated and rotated with respect to the coordinate system, we only need to rotate the $\vec{e}_x$, $\vec{e}_y$, and $\vec{e}_z$ and specify $\vec{c}$. For different blaze angles, we need to tilt the torus differently, leading to different $\vec{e}_x$, $\vec{e}_y$, and $\vec{e}_z$ and different $\vec{c}$. For this spectrograph we chose a $r = 4810$ mm, and $R = 4773$ mm. The vectors defined above are $\vec{c} = (36.2, 588.3, 0)$, $\vec{e}_x = (0.998, -0.061, 0)$, $\vec{e}_y = (0.061, 0.0998, 0)$, and $\vec{e}_z = (0, 0, 1)$.

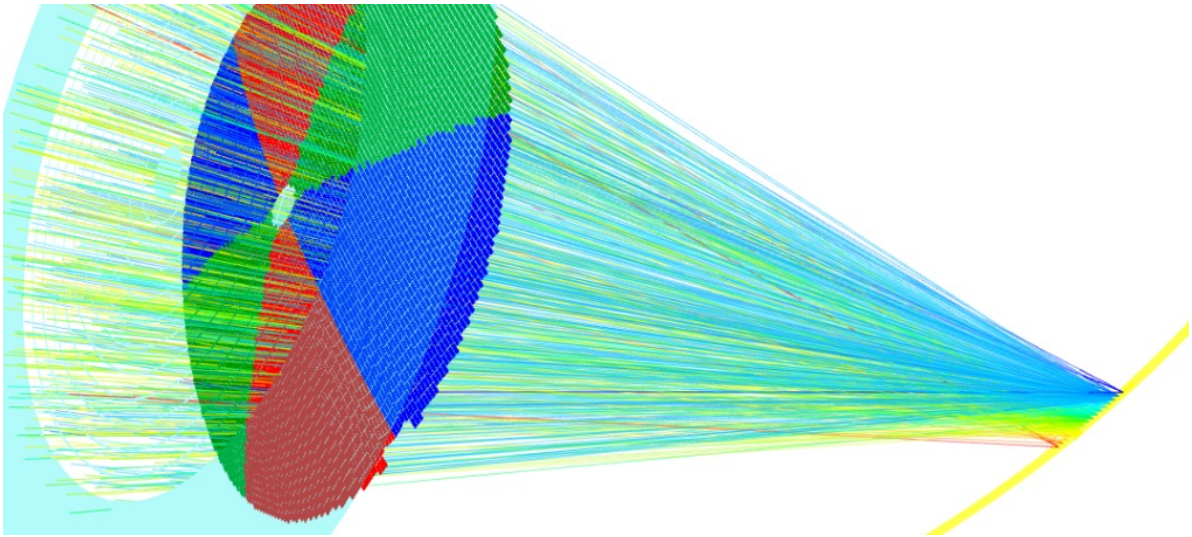

Figure 1. Ray-trace simulation of Lynx XGS. The red, green, and blue rectangles are the active arrea of the CAT gratings. They are arranged on the surface of the Rowland torus. The yellow strip on the right marks the Rowland circle, where the detectors are located (detectors will only be placed on a very small fraction of the yellow strip shown here). Lines show the path or rays through the system. The simulation is monoenergetic. The different colors of the lines indicate into which diffraction order the photons are diffracted. Only photons that pass the gratings and hit the detector are shown, not those that are absorbed by e.g. support structures.

4. SETUP OF RAY-TRACE

We use the MARXS code for our ray-trace.[10,11] MARXS is a Python-based ray-trace code that is available under an open-source license at https://github.com/chandra-marx/marxs. Code specifically for the Lynx can be found at https://github.com/hamogu/marxs-lynx/. The MARXS code is tested with hundreds of unit tests and also verified by comparison to laboratory data and Chandra observations. MARXS performs a geometric ray-trace. Optical properties as discussed in section 2 are read in from data tables.

5. RESULTS

5.1 Position of detector

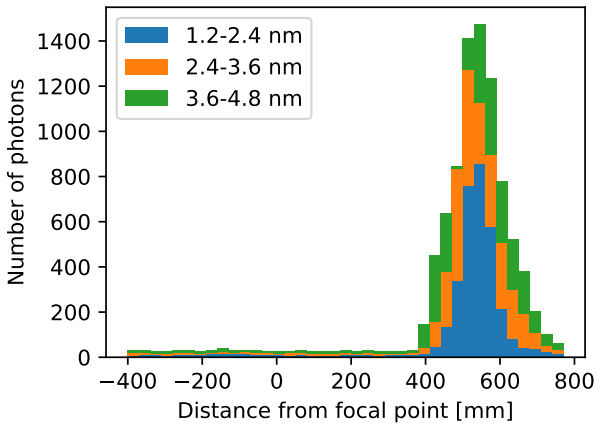

Figure 2. Histrogram of diffracted photon positions on the Rowland circle for a simulation with a continum source. The zeroth order is located at 0 mm.

Figure 2 shows a histogram of the position of diffracted photons for a simulation with a flat input spectrum. The blaze peak where most photons end up is clearly visible. The position and the width of this blaze peak can be derived directly from the input data on the grating efficiencies, but it is useful to check this with a ray-trace to see how non-ideal effects broaden the peak. Because the grating facets are flat, but the photon beam is converging, the nominal blaze angle is only realized in the center of the grating, while all other rays have slightly different blaze angles.

The figure shows that the photon distribution peaks about 550 mm from the zeroth order. In the following we will assume a detecor consisting of 8 CCDs that span from 400 to 800 mm to capture the dispersed signal. We note however, that most of the photons are found in a much narrower range. If the number of CCDs must be reduced because of the size of the dewar around the mirocalorimeter or to reduce cost, power consumption and telemetry, the number of detected photons (i.e. $A_{\rm eff}$) is almost as large for a detector from 450 to 700 mm that would require only 5 CCDs.

5.2 Grating size, mirror properties and sub-aperturing

We define the resolving power as: $R = \frac{\lambda}{\Delta\lambda} = \frac{d_x}{FWMH}$ where λ is the wavelength of a spectral line with negligible intrinsic width, and $\Delta\lambda$ is the observed width of this feature. Since the detector does not give the wavelength directly, d_x and the $FWHM$ are linear distances measured as follows: Events that hit a CCD are projected (not propagated, that would bring them out of focus) into a plane. The $FWMH$ is the full width at half maximum of the event distribution and d_x is the distance between the center of a diffracted order and the zeroth order.

Figure 3 shows the distribution of 0.6 keV photons diffracted into the 6th order for three different scenarios. The bottom right panel shows the distribution for a simulations that uses flat gratings of size 50 mm $\times$ 50 mm with a mirror dominated by off-center error. The top right and bottom left panel are for simulations with gratings of size 50 mm $\times$ 20 mm where the short side is in the dispersion direction and the long side in the cross-dispersion direction. One of the simulations uses the same mirror dominated by off-center error as the 50 mm $\times$ 50 mm simulation, the other one a mirror dominated by figure errors and particulate scattering, where the scatter in the plane of the reflection is five times larger than the scatter in the perpendicular, out-of-plane direction. In all cases, the σ of the Gaussian function describing the random scatter is chosen to get a zero-order PSF with HPD of 0.5 arcsec. The top left plot in the figure shows the position of the gratings in the aperture plane. Gratings are colored according to the angle from the dispersion direction. In the other three panels, photons are colored according to the grating they passed through. We see on all plots that the photons marked in red (gratings along the negative dispersion direction) make the widest distribtion in dispersion direction (x-axis in the plots). Yellow and purple photons are less wide and the narrowest distribution, and thus the best spectral resolving power, is seen for photons passing through the green and dark blue gratings. The light blue photons are wider again than the dark blue or green photons, in particular in the bottom left plot which shows a simulation where the off-center error for the mirrors is small. (This is somewhat hard to see in the image because of the many overlapping dots.) However, the distribution of light blue dots is much narrower than the distribution of red dots. Due to the tilt of the Rowland torus, these two sides are not symmetric. The deviation from the Rowland torus is larger for gratings with a negative coordinate in dispersion direction. For the grating sizes shown here this dominates the spread of the line-spread function (LSF) over the contribution from the mirror PSF alone.

Figure 3 thus demonstrates how subaperturing can be used to improve R: If not the entire aperture is filled with gratings but only a fraction we can achieve a higher R. For example, if only the dark blue and green gratings in figure 3 are inserted into the beam, while the red and light blue ones are not, fewer photons will be detected in the dispersed orders, but the distribution of photons will be narrower leading to a better R.

Figure 4 shows this trade-off in more detail for the three different scenarios. For each sub-aperture angle, we calculate R and $A_{\rm eff}$. A higher R goes along with using fewer gratings and thus a lower $A_{\rm eff}$. 50 mm $\times$ 20 mm gratings can deliver $R > 5000$ for both mirror scenarios we simulate here, while 50 mm $\times$ 50 mm gratings deliver R below the requirements for all sub-aperturing angles that provide $A_{\rm eff} > 4000$ cm^2.

At this early stage of development, we need to plan for a resolving power that is above the minimum requirement, since in practice the number for R will degrade due to misalignments during grating mounting and the assembly of the XGS. If larger misalignments are tolerable, the assembly will be quicker, faster and cheaper since fewer detailed alignment steps are required.

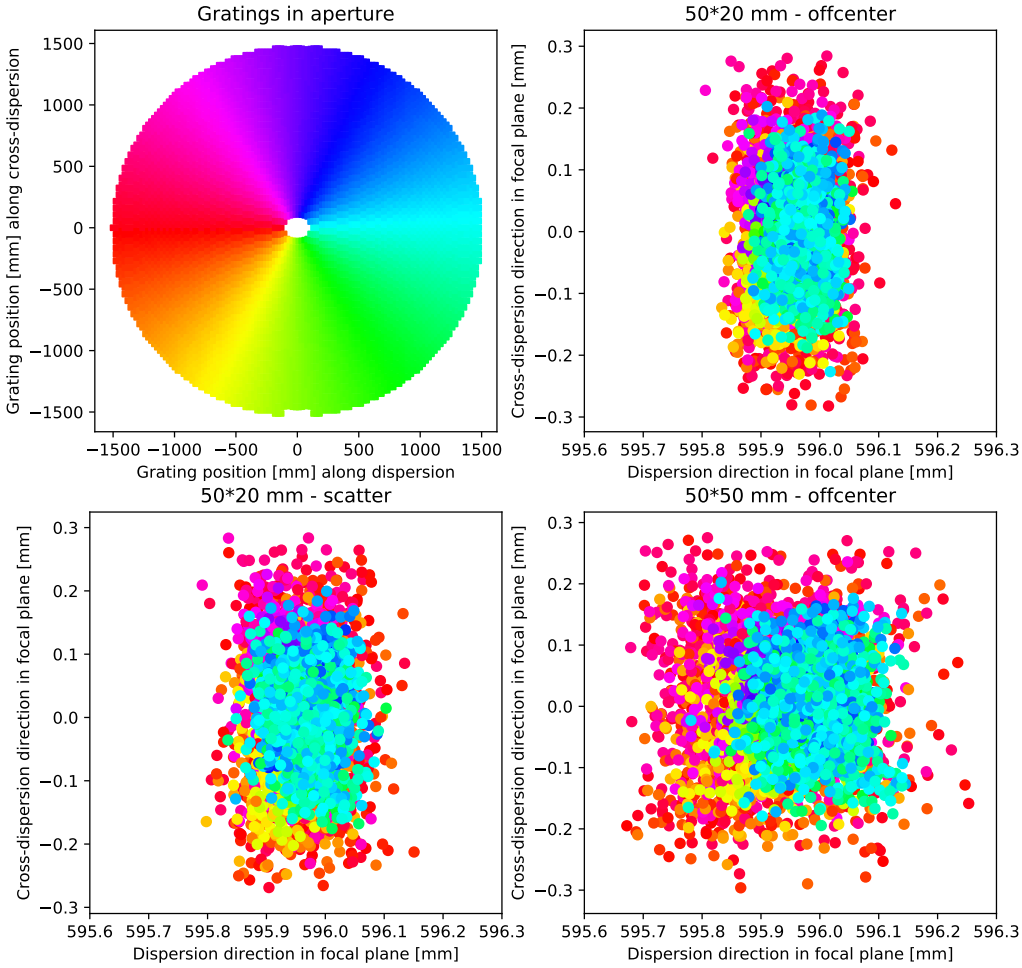

Figure 3. *top left:* Position of gratings in the aperture plane. The placement of gratings is so dense that they appear continutous in this plot, but in reality there is space for 1 mm wide frame around each grating. The gratings are color coded by angle relative to the dispersion direction (positive x-axis). *top right and bottom:* Distribution of photons in the sixth order for different CAT grating sizes and mirror scattering properties. Each dot represents a single detected photon, color coded by the grating it passed.

On the other hand, the simulations shown in figure 4 assume a very simple sub-aperturing strategy, where gratings are added equally to the left and to the right, starting from the horizontal $x = 0$ line in figure 3 (top left panel). As shown in the other panels of that figure, the broadening of the line is not symmetric between the positive and negative x-axis, so a better sub-aperturing strategy would be to add more gratings to the right than to the left, which will improve R.

5.3 Effective area and resolving power over the XGS bandpass

In the previous section, we presented simulations at 0.6 keV, because the science requirements for the XGS are defined at this energy. We now present results for the grid of energies. Since the mirror properties are provided to us at only a small number of energies, the grid is not very dense.

Figure 5 shows $A_{\rm eff}$ and R for different sub-aperturing angles. The angles given in the figure are the half-opening angles for one wedge. In other words, a sub-aperturing angle of 45 degrees means a wedge ranging from -45 to + 45 degrees from the centerline, i.e. the wedge is 90 degrees wide. Because of the symmetry around the dispersion direction (x-axis in figure 3, top left) there should be a total of two wedges. The second wedge has

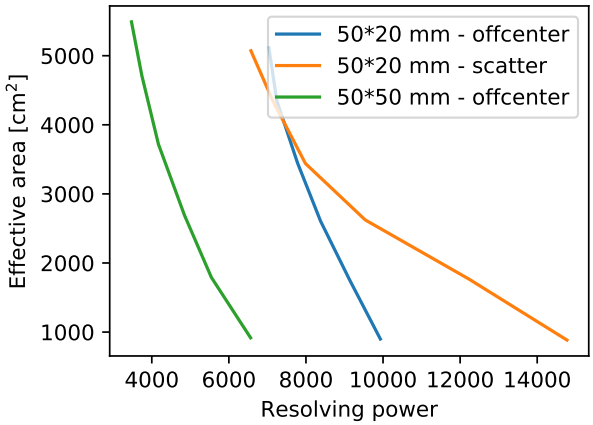

Figure 4. Trade-off between R and $A_{\rm eff}$ for different grating sizes and mirror scenarios for observations at 0.6 keV.

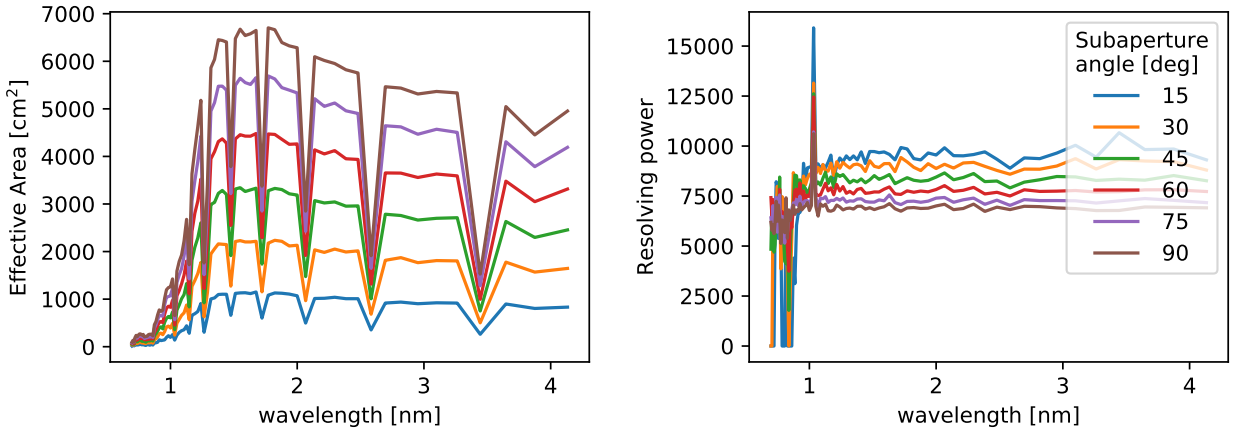

Figure 5. $A_{\rm eff}$ and R for different subaperturing angles. See text for an explanation of the angles listed in the legend.

equal size, so a half-opening angle of 45 degrees on each of them means that one half of the total aperture is covered with gratings and a half-opening angle of 90 degrees corresponds to an aperture covered entirely with gratings.

The figure shows that $A_{\rm eff}$ is low for short wavelengths. For this reason, the plot of R is very noisy in this region - there are just too few diffracted photons in the Monte-Carlo simulation to reliably determine R. The $A_{\rm eff}$ given in the figure is the total effective area summed over all diffraction orders that are detected on the CCDs defined in section 5.1. Some chip gaps are visible in the plot of $A_{\rm eff}$, but the wavelength grid is too coarse to study them in detail. Since more than one order is detected for most wavelengths, the chip gaps generally lead to a reduced, but still non-zero $A_{\rm eff}$ at that wavelength. A Chandra-like dither pattern could be employed to reduce their impact.

A sub-aperturing angle of 60 degrees will deliver the $A_{\rm eff}$ and R to fulfill the science requirements of the XGS.

5.4 Usability of the zeroth order

An important question is how the presence of the gratings interferes with observations in the zeroth order simultaneous to the grating data. The position of the zeroth order is required for wavelength calibration of the diffracted signal, but especially at energies above 2 keV where $A_{\rm eff}$ of the dispersed orders is low, analysis of the zero order microcalorimeter data becomes important. For example, in young, flaring stars it would be possible to study the mass accretion in the soft-X-rays in the diffracted signal and the hot Fe Kα line in the microcalorimeter

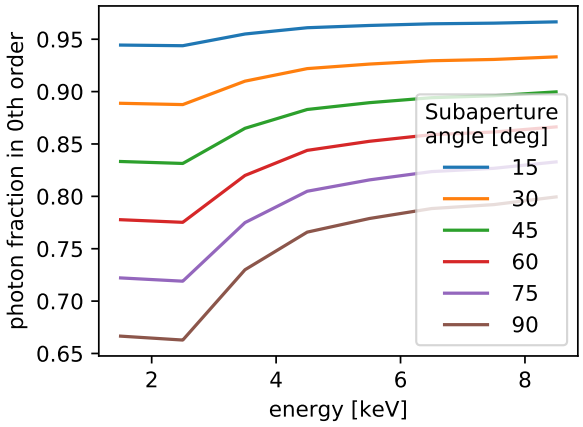

Figure 6. Fraction of photons observed in zeroth order for different fillings of the aperture plane with gratings. The fraction shown takes into account the areas of the plane not covered by gratings and the fraction of photons that pass through the gratings in those locations where gratings are mounted.

simultaneously. Figure 6 shows that the CAT gratings are mostly transparent at energies so high that the signal is not diffracted efficiently any longer. For the scenario of 60 degree half-angle of the wedge filled with CAT gratings (i.e. two-thirds of the aperture are covered with CAT gratings) only 15-20% of the high-energy photons are absorbed - and these simulations already include absorption by the mounting structure of the gratings.

6. DESIGN OPTIONS

In the previous sections, we show that a relatively simple design fulfills the science requirements on the XGS as they are defined in early 2018. In this section, we want to discuss design options that could improve the capability of the instrument at the cost of a slightly more complex design. It is beyond the scope of the current proceedings to perform a detailed trade study on each of them.

6.1 Detailed grating placement

In figures 1 and 3 gratings are placed to homogeneously fill the area behind the mirrors and each grating has space for a 1 mm wide mounting frame. In practice, a structure as large as the XGS grating assembly will need a few thicker and more substantial support structures which will introduce wider shadows. On the other hand, the mirror effective area is not equally distributed over the entire area either. The mounting structures of the grating assembly should be aligned with the support structures of the mirror to reduce the area lost. A detailed study of this cannot be performed before the mirror is better specified, but our experience from the detailed Arcus design and ray-tracing in Phase 1 (see Günther et al in this volume) is that this will have negligible impact on R and will change $A_{\rm eff}$ by a few percent at most.

6.2 Coated gratings

The simulations above assume uncoated Si CAT gratings. Coating the surface of these gratings with a metal, e.g. Pt,[12] would increase the grating efficiency at higher energies and thus significantly improve the effective area of the XGS at short wavelength. At the same time, those photons would be lost from the zeroth order, reducing the effective area for high-energy photons there. It is not beneficial to coat all gratings, because for high energies the microcalorimeter used as zeroth-order detector delivers better spectra than a CAT grating. However, if even a small fraction of gratings is coated, the effective area below 12 Å could already be increased by a factor of a few.

6.3 Two grating traces

Figure 4 shows how the resolving power decreases as more and more gratings are used because that means some of them must be placed at sub-aperturing angles which are not ideal. This problem can be overcome by generating two spectral traces on the detector, similar to how it is done in Chandra/HETG,[13] where the gratings that make up the High-Energy Grating (HEG) and the Medium-Energy grating (MEG) are mounted such that their dispersion directions differ a little. The resulting signal is an X on the detector, where one diagonal belongs to each of the respective gratings. In the Lynx XGS, we would rotate the dispersion direction for a fraction of the gratings that are located at the best subaperturing angles (as judged from ray-tracing pre-flight) by 0.5 degrees and the remaining gratings by -0.5 degrees. That would give us two traces on the CCD array which are diverging with an average distance of 10 mm – more than enough to separate them easily, but still far away from the detector edges. Similar to Chandra/HETG, the data reduction software would extract two separate spectra and the observer could choose to analyze only one spectrum with the highest R, but limited $A_{\rm eff}$ for science questions that require the best spectral resolution, or fit them jointly to take advantage of the full effective area. The main drawback of this approach is that it is more likely that spectra overlap for observations of crowded fields, like the Orion Nebula Cloud, where many targets may produce bright grating spectra, but those targets will be difficult to observe and reduce in any case.

In principle, even three or more traces are possible, but the difference in resolving power between each of them would not be large, and likely not warrant the additional complexity. Also, the smaller $A_{\rm eff}$ in each spectral trace is, the higher is the relative detector background.

A variant of this idea is to mount the gratings on several different sectors that can be moved into the beam independently, e.g. in sectors that are 30 degrees wide. In that case, an observer might specify to insert only the gratings in the -15 to +15 degree sector, while another observation could be done with the gratings in the sectors -45 to -15, -15 to +15, and +15 to +45 degrees. This would lower the resolving power, but deliver three times the effective area.

6.4 Chirp

If CAT gratings are produced with projection lithography, there is more freedom to chose parameters than in the current process.[14] In particular, it is possible to vary the grating period from one end of the grating facet to the other. This can be used to somewhat compensate the fact that gratings of finite size muss differ from the surface of the Rowland torus. For gratings of fixed size, this would increase R, or when keeping a fixed requirement of R gratings could be manufactured larger, thus reducing the number of gratings needed (and thus the cost) and also the area lost to the mounting structures that hold the gratings in place, and thus increase $A_{\rm eff}$. This requires a more detailed ray-trace study to evaluate the impact on the design and to chose the best chirp parameters.

7. SUMMARY

We present a design and ray-traces for an X-ray grating spectrograph on Lynx. We describe the assumptions going into our design, one of which is the effective area of the Lynx mirrors, and show that CAT gratings covering about two thirds of the total area can disperse a spectrum onto a small number of CCDs with $R > 5000$ and $A_{\rm eff} > 4000$ cm^2 at an energy of 0.6 keV and can thus meet the Lynx science requirements for a grating spectrograph.

ACKNOWLEDGMENTS

Support for this work was provided in part through Smithsonian Astrophysical Observatory (SAO) contract SV3-73016 to MIT for support of the *Chandra* X-Ray Center (CXC), which is operated by SAO for and on behalf of NASA under contract NAS8-03060. The simulations make use of Astropy, a community-developed core Python package for Astronomy,[15,16] numpy,[17] and IPython.[18] Displays are done with mayavi[19] and matplotlib.[20]

REFERENCES

[1] Collon, M. J., Vacanti, G., Gnther, R., Yanson, A., Barrire, N., Landgraf, B., Vervest, M., Chatbi, A., Beijersbergen, M. W., Bavdaz, M., Wille, E., Haneveld, J., Koelewijn, A., Leenstra, A., Wijnperle, M., van Baren, C., Mller, P., Krumrey, M., Burwitz, V., Pareschi, G., Conconi, P., and Christensen, F. E., "Silicon pore optics development for athena," *Proc. SPIE* **9603**, 96030K–96030K–11 (2015).

[2] Collon, M. J., Ackermann, M., Günther, R., Chatbi, A., Vacanti, G., Vervest, M., Yanson, A., Beijersbergen, M. W., Bavdaz, M., Wille, E., Haneveld, J., Olde Riekerink, M., Koelewijn, A., van Baren, C., Müller, P., Krumrey, M., Burwitz, V., Sironi, G., and Ghigo, M., "Making the athena optics using silicon pore optics," *Proc. SPIE* **9144**, 91442G–91442G–8 (2014).

[3] Gaskin, J. A., Allured, R., Bandler, S. R., Basso, S., Bautz, M. W., Baysinger, M. F., Biskach, M. P., Boswell, T. M., Capizzo, P. D., Chan, K.-W., Civitani, M. M., Cohen, L. M., Cotroneo, V., Davis, J. M., DeRoo, C. T., DiPirro, M. J., Dominguez, A., Fabisinski, L. L., Falcone, A. D., Figueroa-Feliciano, E., Garcia, J. C., Gelmis, K. E., Heilmann, R. K., Hopkins, R. C., Jackson, T., Kilaru, K., Kraft, R. P., Liu, T., McClelland, R. S., McEntaffer, R. L., McCarley, K. S., Mulqueen, J. A., Özel, F., Pareschi, G., Reid, P. B., Riveros, R. E., Rodriguez, M. A., Rowe, J. W., Saha, T. T., Schattenburg, M. L., Schnell, A. R., Schwartz, D. A., Solly, P. M., Suggs, R. M., Sutherlin, S. G., Swartz, D. A., Trolier-McKinstry, S., Tutt, J. H., Vikhlinin, A., Walker, J., Yoon, W., and Zhang, W. W., "Lynx mission concept status," *Proc.SPIE* **10397**, 10397 – 10397 – 13 (2017).

[4] Heilmann, R. K., Ahn, M., Bruccoleri, A., Chang, C.-H., Gullikson, E. M., Mukherjee, P., and Schattenburg, M. L., "Diffraction efficiency of 200-nm-period critical-angle transmission gratings in the soft x-ray and extreme ultraviolet wavelength bands," *Appl. Opt.* **50**, 1364–1373 (Apr 2011).

[5] Heilmann, R. K., Bruccoleri, A. R., and Schattenburg, M. L., "High-efficiency blazed transmission gratings for high-resolution soft x-ray spectroscopy," *Proc. SPIE* **9603**, 960314–960314–12 (2015).

[6] Smith, R. K., Abraham, M., Allured, R., Bautz, M., Bookbinder, J., Bregman, J., Brenneman, L., Brickhouse, N. S., Burrows, D., Burwitz, V., Cheimets, P. N., Costantini, E., Dawson, S., DeRoo, C., Falcone, A., Foster, A. R., Gallo, L., Grant, C. E., Gnther, H. M., Heilmann, R. K., Hertz, E., Hine, B., Huenemoerder, D., Kaastra, J. S., Kreykenbohm, I., Madsen, K. K., McEntaffer, R., Miller, E., Miller, J., Morse, E., Mushotzky, R., Nandra, K., Nowak, M., Paerels, F., Petre, R., Poppenhaeger, K., Ptak, A., Reid, P., Sanders, J., Schattenburg, M., Schulz, N., Smale, A., Temi, P., Valencic, L., Walker, S., Willingale, R., Wilms, J., and Wolk, S. J., "Arcus: exploring the formation and evolution of clusters, galaxies, and stars," *Proc.SPIE* **10397**, 10397 – 10397 – 11 (2017).

[7] Beuermann, K. P., Bräuninger, H., and Trümper, J., "Aberrations of a facet-type transmission grating for cosmic x-ray and xuv spectroscopy," *Appl. Opt.* **17**, 2304–2309 (Aug 1978).

[8] Heilmann, R. K., Davis, J. E., Dewey, D., Bautz, M. W., Foster, R., Bruccoleri, A., Mukherjee, P., Robinson, D., Huenemoerder, D. P., Marshall, H. L., Schattenburg, M. L., Schulz, N. S., Guo, L. J., Kaplan, A. F., and Schweikart, R. B., "Critical-angle transmission grating spectrometer for high-resolution soft x-ray spectroscopy on the international x-ray observatory," *Proc. SPIE* **7732**, 77321J–77321J–11 (2010).

[9] Günther, H. M., Cheimets, P. N., Heilmann, R. K., and Smith, R. K., "Performance of a double tilted-rowland-spectrometer on arcus," *Proc.SPIE* **10397**, 10397 – 10397 – 12 (2017).

[10] Günther, H. M., Frost, J., , and Theriault-Shay, A., "Chandra-marx/marxs: v1.1," (Jul 2017).

[11] Günther, H. M., Frost, J., and Theriault-Shay, A., "MARXS: A Modular Software to Ray-trace X-Ray Instrumentation," *AJ* **154**, 243 (Dec. 2017).

[12] Heilmann, R. K., Bruccoleri, A. R., Kolodziejczak, J., Gaskin, J. A., O'Dell, S. L., Bhatia, R., and Schattenburg, M. L., "Critical-angle x-ray transmission grating spectrometer with extended bandpass and resolving power $> 10,000$," *Proc. SPIE* **9905**, 99051X–99051X–12 (2016).

[13] Canizares, C. R., Davis, J. E., Dewey, D., Flanagan, K. A., Galton, E. B., Huenemoerder, D. P., Ishibashi, K., Markert, T. H., Marshall, H. L., McGuirk, M., Schattenburg, M. L., Schulz, N. S., Smith, H. I., and Wise, M., "The Chandra High-Energy Transmission Grating: Design, Fabrication, Ground Calibration, and 5 Years in Flight," *PASP* **117**, 1144–1171 (Oct. 2005).

[14] Song, J., Heilmann, R. K., Bruccoleri, A. R., Hertz, E., and Schatternburg, M. L., "Scanning laser reflection tool for alignment and period measurement of critical-angle transmission gratings," *Proc.SPIE* **10399**, 10399 – 10399 – 10 (2017).

[15] Astropy Collaboration, Robitaille, T. P., Tollerud, E. J., Greenfield, P., Droettboom, M., Bray, E., Aldcroft, T., Davis, M., Ginsburg, A., Price-Whelan, A. M., Kerzendorf, W. E., Conley, A., Crighton, N., Barbary, K., Muna, D., Ferguson, H., Grollier, F., Parikh, M. M., Nair, P. H., Günther, H. M., Deil, C., Woillez, J., Conseil, S., Kramer, R., Turner, J. E. H., Singer, L., Fox, R., Weaver, B. A., Zabalza, V., Edwards, Z. I., Azalee Bostroem, K., Burke, D. J., Casey, A. R., Crawford, S. M., Dencheva, N., Ely, J., Jenness, T., Labrie, K., Lim, P. L., Pierfederici, F., Pontzen, A., Ptak, A., Refsdal, B., Servillat, M., and Streicher, O., "Astropy: A community Python package for astronomy," *A&A* **558**, A33 (Oct. 2013).

[16] The Astropy Collaboration, Price-Whelan, A. M., Sipőcz, B. M., Günther, H. M., Lim, P. L., Crawford, S. M., Conseil, S., Shupe, D. L., Craig, M. W., Dencheva, N., Ginsburg, A., VanderPlas, J. T., Bradley, L. D., Pérez-Suárez, D., de Val-Borro, M., Aldcroft, T. L., Cruz, K. L., Robitaille, T. P., Tollerud, E. J., Ardelean, C., Babej, T., Bachetti, M., Bakanov, A. V., Bamford, S. P., Barentsen, G., Barmby, P., Baumbach, A., Berry, K. L., Biscani, F., Boquien, M., Bostroem, K. A., Bouma, L. G., Brammer, G. B., Bray, E. M., Breytenbach, H., Buddelmeijer, H., Burke, D. J., Calderone, G., Cano Rodríguez, J. L., Cara, M., Cardoso, J. V. M., Cheedella, S., Copin, Y., Crichton, D., DÁvella, D., Deil, C., Depagne, É., Dietrich, J. P., Donath, A., Droettboom, M., Earl, N., Erben, T., Fabbro, S., Ferreira, L. A., Finethy, T., Fox, R. T., Garrison, L. H., Gibbons, S. L. J., Goldstein, D. A., Gommers, R., Greco, J. P., Greenfield, P., Groener, A. M., Grollier, F., Hagen, A., Hirst, P., Homeier, D., Horton, A. J., Hosseinzadeh, G., Hu, L., Hunkeler, J. S., Ivezić, Ž., Jain, A., Jenness, T., Kanarek, G., Kendrew, S., Kern, N. S., Kerzendorf, W. E., Khvalko, A., King, J., Kirkby, D., Kulkarni, A. M., Kumar, A., Lee, A., Lenz, D., Littlefair, S. P., Ma, Z., Macleod, D. M., Mastropietro, M., McCully, C., Montagnac, S., Morris, B. M., Mueller, M., Mumford, S. J., Muna, D., Murphy, N. A., Nelson, S., Nguyen, G. H., Ninan, J. P., Nöthe, M., Ogaz, S., Oh, S., Parejko, J. K., Parley, N., Pascual, S., Patil, R., Patil, A. A., Plunkett, A. L., Prochaska, J. X., Rastogi, T., Reddy Janga, V., Sabater, J., Sakurikar, P., Seifert, M., Sherbert, L. E., Sherwood-Taylor, H., Shih, A. Y., Sick, J., Silbiger, M. T., Singanamalla, S., Singer, L. P., Sladen, P. H., Sooley, K. A., Sornarajah, S., Streicher, O., Teuben, P., Thomas, S. W., Tremblay, G. R., Turner, J. E. H., Terrón, V., van Kerkwijk, M. H., de la Vega, A., Watkins, L. L., Weaver, B. A., Whitmore, J. B., Woillez, J., and Zabalza, V., "The Astropy Project: Building an inclusive, open-science project and status of the v2.0 core package," *ArXiv e-prints* (Jan. 2018).

[17] van der Walt, S., Colbert, S. C., and Varoquaux, G., "The numpy array: A structure for efficient numerical computation," *Computing in Science & Engineering* **13**(2), 22–30 (2011).

[18] Pérez, F. and Granger, B. E., "IPython: a system for interactive scientific computing," *Computing in Science and Engineering* **9**, 21–29 (May 2007).

[19] Ramachandran, P. and Varoquaux, G., "Mayavi: 3D Visualization of Scientific Data," *Computing in Science & Engineering* **13**(2), 40–51 (2011).

[20] Hunter, J. D., "Matplotlib: A 2d graphics environment," *Computing In Science & Engineering* **9**(3), 90–95 (2007).